PCCP

PAPER

View Article Online
View Journal | View Issue

Cite this: *Phys. Chem. Chem. Phys.*, 2025, **27**, 25098

UV-A scintillation and persistent luminescence from Ce- and Ce/Ho-doped YPO_4 nanoparticles

Paul Ganigal,[a] David Van der Heggen,[b] Philippe F. Smet,[b] Christophe Dujardin,[c] Mathilde Ménard,[a] Christophe Dorandeu,[a] Jean-Olivier Durand[a] and Aurélie Bessière*[a]

Received 12th July 2025,
Accepted 11th October 2025

DOI: 10.1039/d5cp02667a

rsc.li/pccp

Ce^{3+}- and Ce^{3+}/Ho^{3+}-doped YPO_4 nanoparticles were synthesized *via* a microwave-assisted hydrothermal method to explore their potential as UV-A (320–400 nm) emitting nanoscintillators and persistent luminescence nanophosphors. The as-prepared Ce-doped YPO_4 nanoparticles exhibited nanoporosity, a median size of ∼55 nm, and detectable Ce^{3+} photoluminescence (PL) without the need for high-temperature annealing. Post-synthesis annealing at 1100 °C markedly enhanced both the PL yield and radioluminescence (RL) response, achieving ∼37% of the RL intensity observed in a bulk reference sample. This enhancement was accompanied by a moderate increase in particle median size to ∼68 nm and a loss of nanoporosity. Under X-ray excitation, the annealed nanoparticles demonstrated fast scintillation with a main decay time of ∼27 ns. Co-doping with Ho^{3+} induced persistent UV-A luminescence, supporting the roles of Ce^{3+} as a deep hole trap and Ho^{3+} as a shallower electron trap. Optimal persistent luminescence was observed at nominal Ce/Ho concentrations of 0.5/0.5 mol%. These findings highlight the dual-mode optical functionality of Ce- and Ce/Ho-doped YPO_4 nanoparticles, offering rapid scintillation response and long-lasting emission, respectively. Combined with the already reported structural stability, biocompatibility, and aqueous dispersibility of the YPO_4 nanoparticles, these materials are promising candidates for biomedical applications requiring sustained UV-A emission in deep tissue environments.

1. Introduction

The xenotime phase of YPO_4 is considered an attractive host matrix for the design of inorganic phosphors, as it demonstrates a high capacity for incorporating dopant ions, particularly lanthanide ions (Ln^{3+}) with similar oxidation states as the host Y^{3+} ions. Furthermore, one of its major advantages lies in its physico-chemical robustness: it is chemically stable, non-hygroscopic, and highly resistant to thermal degradation.[1] Because of these attributes, Ln^{3+}-doped YPO_4 crystals and microcrystalline powders have been initially proposed for a range of applications, including plasma display panels,[2] laser host materials,[3] and scintillators.[4,5] As a single crystal, the Ce^{3+}-doped YPO_4 scintillator does not achieve the highest light yields compared to benchmark crystals like $Lu_{(2-x)}Y_xSi_2O_5$:Ce (LYSO)[4] or $Gd_3Al_2Ga_3O_{12}$:Ce (GAGG).[6] It also exhibits lower density (ρ = 4.5 g cm^{-3}) and an effective atomic number (Z_{eff} ∼ 16) than top-performing scintillators for X-ray or PET imaging such as $Bi_4Ge_3O_{12}$ (BGO),[7] LYSO,[8] or Gd_2SiO_5:Ce (GSO).[9] Nevertheless, YPO_4:Ce remains an attractive scintillating material due to its physico-chemical robustness and its 30 ns-fast scintillation response time.[5,10] Furthermore, its Z_{eff} can easily be increased by shifting to $LuPO_4$.

On the other hand, the presence of a single crystallographic site in the xenotime structure of YPO_4 has established it as a perfect model host for systematically investigating and predicting the energy level positions of Ln^{3+} and Ln^{2+} lanthanide ions relative to the valence and conduction bands of the matrix, as shown in Fig. S2.[11] These insights have significantly advanced the understanding of the optical behaviour of lanthanide-doped YPO_4. In particular, they enable the prediction and interpretation of electron and hole trapping processes that precede radiative recombination at Ln^{3+} or Ln^{2+} centers.[12–14] In the past, we have applied this knowledge to the rational design of novel X-ray-activated, red-emitting persistent phosphors based on YPO_4:Pr^{3+},Ln^{3+} (Ln = Nd^{3+}, Dy^{3+}, Ho^{3+}, or Er^{3+}).[15] In these systems, Pr^{3+} serves both as a stable hole trap and as a red emitter through the $^1D_2 \rightarrow {}^3H_4$, $^3P_0 \rightarrow {}^3H_6$, and $^3P_0 \rightarrow {}^3F_2$ $4f^2$–$4f^2$ transitions. Meanwhile, co-doping the YPO_4 host matrix with trivalent lanthanide ions such as Nd^{3+}, Dy^{3+},

---

[a] *ICGM, CNRS UMR 5253, Université Montpellier, ENSCM, Montpellier 34293, France. E-mail: aurelie.bessiere@umontpellier.fr*
[b] *LumiLab, Dept. Solid State Sciences, Ghent University, Ghent, Belgium*
[c] *Institut Lumière Matière, CNRS UMR 5306, Université Claude Bernard Lyon1, Villeurbanne 69622, France*

Ho^{3+}, or Er^{3+} introduces shallow electron traps, which are directly responsible for the occurrence of persistent luminescence at room temperature. Among the studied co-dopants, Ho^{3+} was found to be the most effective, producing the most intense and longest-lasting persistent luminescence.[15] Similarly to Pr^{3+}, Ce^{3+}, according to thermally stimulated luminescence (TSL) results, is capable of acting as a deep hole trap while emitting in the UV-A range through its 5d–4f transitions.[15–18] Therefore, a tailored combination of Ce^{3+} and Ho^{3+} dopants in the YPO_4 host matrix should enable the induction of persistent luminescence at room temperature in UV-A, underscoring the potential of YPO_4 not only as a scintillating material but also as a UV-A persistent phosphor.

In the past 10–15 years, various synthesis routes have been developed to produce YPO_4 in nanoparticle form. Notably, nanoscale YPO_4 has attracted significant interest due to its low toxicity, excellent biocompatibility, and high dispersibility in aqueous media,[19] making it well-suited for applications such as luminescent bioprobes in biomedical imaging and diagnostics.[20–22] Reported synthesis techniques include sol–gel,[23] polyol,[24] and hydrothermal methods, with[25,26] or without the use of organic additives,[19,27–31] as well as solvothermal methods.[32] Depending on the synthesis conditions, YPO_4 nanoparticles can crystallize in three main structural phases: two hydrated forms—hexagonal rhabdophane ($YPO_4{\cdot}0.8H_2O$) and monoclinic churchite ($YPO_4{\cdot}2H_2O$)—and one anhydrous YPO_4 form, the tetragonal xenotime phase. The latter is often preferred due to its high stability and low coordinated water content, which helps minimize luminescence quenching.[22,33] Notably, this stable tetragonal phase can be directly obtained in nanocrystalline form through appropriate synthesis methods. Among these, hydrothermal and solvothermal synthesis methods stand out as simple, low-temperature, cost-effective, and high-yield routes that offer good control over particle morphology, size, crystal structure, and crystallinity. Even more advantageous is the microwave (MW)-assisted hydrothermal method, which enables rapid reactions, high reproducibility, and enhanced uniformity in particle size and shape.[34,35]

Among the recent studies on luminescent doped YPO_4 nanoparticles, Eu^{3+}- and Tb^{3+}-doped YPO_4 has been the most extensively investigated, consistently demonstrating efficient photoluminescence (PL) in the visible range.[19,25,26,28–31,36–39] As a result, they have been considered promising for biomedical applications such as cell labeling, molecular detection, and bioimaging, as well as for optoelectronic devices, display technologies, and LEDs. In contrast, Ce^{3+} doping has been less explored, as it yields an emission in UV-A. In the few available studies, Ce^{3+} has primarily been used as a sensitizer to enhance the PL of Tb^{3+} or Eu^{3+} under UV excitation,[24,32,33] and only rarely has Ce^{3+} been reported as the sole emitter.[23]

In this study, we developed photoluminescent YPO_4:Ce nanoparticles using a water-based, and environmentally friendly synthesis route based on MW-assisted hydrothermal treatment. To evaluate their potential as nano-scintillators emitting in the UV-A range, we demonstrated that a subsequent thermal treatment at 1100 °C significantly enhanced the scintillation yield under X-ray excitation, while preserving the nanoparticulate morphology. Building on these results, we introduced a Ho^{3+} co-doping strategy to engineer a nanoparticle platform capable of exhibiting persistent luminescence in the UV-A region. Such a nano-platform could be valuable for emitting UV-A deep within biological tissues to trigger biorthogonal photoclick reactions.[40]

2. Experimental

Mono-doped YPO_4:Ce^{3+} and co-doped YPO_4:Ce^{3+},Ho^{3+} nanopowders with varying Ce and Ho contents were synthesized using a MW-assisted hydrothermal method. Stoichiometric amounts of aqueous solutions of $Y(NO_3)_3{\cdot}6H_2O$ (Merck, 99.8% pure), $Ce(NO_3)_3{\cdot}6H_2O$ (Merck, 99.99% pure), and $Ho(NO_3)_3{\cdot}5H_2O$ (Merck, 99.9% pure) were mixed with H_3PO_4 (Thermo, 85% pure) and heated by microwave irradiation in a Discover SP system for 30 minutes at 120 °C. The reaction mixture was centrifuged using an Allegra 64R at 20 000 rpm, and the obtained powder was washed twice with ethanol and distilled water before being dried overnight at 70 °C. Selected samples were subsequently annealed in a tubular furnace at 1100 °C for 5 hours under air flow. The names and synthesis conditions of the prepared samples, labelled with the prefix "MW", along with their Ce and Ho contents relative to the total rare-earth (RE) cation concentration, are summarized in Table 1.

For comparison, mono-doped YPO_4:Ce^{3+} and co-doped YPO_4:Ce^{3+},Ho^{3+} "bulk" powders were synthesized *via* a solid-state reaction (SSR) method. Stoichiometric amounts of Y_2O_3 (Merck, 99.99% purity), CeO_2 (Alfa Aesar, 99.99%), Ho_2O_3 (Merck, 99.999%), and $NH_4H_2PO_4$ (Thermo, 98%) were weighed and thoroughly mixed in an agate mortar. The resulting powder

Table 1 Nominal and experimental (determined by ICP-OES spectroscopy) Ce/RE and Ho/RE (RE = Y + Ce + Ho) molar ratios (%) of the prepared lanthanide-doped yttrium phosphate samples

Sample name	Synthesis method	Host	Nominal Ce/RE	Exp. Ce/RE	Nominal Ho/RE	Exp. Ho/RE
MW-AP	MW-assisted hydrothermal synthesis	YPO_4	0.5	0.24	—	—
MW-1	MW-assisted hydrothermal synthesis followed by annealing at 1100 °C			0.24	—	—
MW-2				0.40	0.5	0.59
MW-3				0.42	1	1.11
MW-4				0.42	2	1.89
SSR-1	SSR at 1400 °C		0.3	0.35	—	—
SSR-2	SSR at 1100 °C	$Y(PO_3)_3$	0.5	NA	—	NA

was pelletized and subjected to a first thermal treatment in a muffle furnace at 400 °C for 10 hours. After cooling, the pellets were ground, pelletized again, and annealed a second time in a tubular furnace at 1400 °C for 4 hours under argon flow. The sample names, prefixed "SSR," along with their synthesis conditions and Ce and Ho contents relative to the total RE cation content, are summarized in Table 1.

Inductively coupled plasma-optical emission spectrometry (ICP-OES) analyses were performed using an iCap 7400 Duo Thermo Fisher equipment. Compounds were digested in hot nitric acid using a Katanax X-600 fluxer prior to dilution for analysis.

X-ray diffraction (XRD) studies were performed using a PANalytical X'Pert Powder analytical diffractometer mounted in a Debye–Scherrer configuration and equipped with a copper cathode (λ = 1.5418 Å). The diffractograms were recorded in the 2θ range of 15°–75° with a 0.03° step size and a scan speed of 1.2° min^{-1}.

Fourier-transform infrared spectroscopy (FT-IR) spectra were recorded using a Spectrum Two FT-IR spectrometer used in ATR mode in the range of 4000 cm^{-1} to 400 cm^{-1}.

Scanning electron microscopy (SEM) measurements were conducted on a Hitachi S4800 instrument under an excitation voltage ranging from 0.5 to 8.0 kV, depending on the surface charging of each powder. Powdered compounds were deposited on double-sided conducting carbon tape and then platinum-metallized by sputtering under vacuum.

Transmission electron microscopy (TEM) was performed on a JEOL 1200EX transmission electron microscope, using an accelerating voltage of 120 kV.

Nitrogen adsorption and desorption isotherms were recorded at 77 K using a Micromeritics 3Flex apparatus after outgassing the samples overnight at 150 °C (10^{-3} Torr). The Brunauer–Emmett–Teller (BET) method was used to calculate the specific surface areas of the samples, and the pore size distributions were calculated using the Barrett–Joyner–Halenda (BJH) method.

Room temperature PL spectra were recorded on a FLS920P spectrofluorometer with a xenon lamp (450 W) as the excitation source. The powders were loaded into a 1 mm-thick sample holder, which was sealed with a quartz window to keep the powder in place even in a vertical orientation. In this configuration, the sample surface was vertical, while the incident excitation beam was horizontal. The beam always illuminated the same sample area at a 45° angle of incidence.

Luminescence decay times were measured using two different excitation sources. For UV excitation, a DeltaDiode DD-325 from Horiba, emitting at 325 nm, was used. The excitation beam was spectrally cleaned with a bandpass optical filter centered at 326 nm (ref. 326FS01, Andover Corporation). For X-ray excitation, a pulsed diode DeltaDiode-405L from Horiba, emitting at 405 nm, was used to illuminate the photocathode of an X-ray tube (model N5084, Hamamatsu) operated at 35 kV. In both cases, the excitation repetition rate was set to 500 kHz. The emitted light was collected through a shortpass filter at 350 nm (ref. 350SC01, Andover Corporation). Detection was performed using a PMA-C photomultiplier tube (PicoQuant). Time-resolved measurements were carried out using a PicoHarp 300 time-correlated single photon counting system (PicoQuant), set with a time resolution of 256 ps per channel. Each decay curve was recorded over a time window of 2 μs.

Radioluminescence (RL) spectra were measured using a miniX2 X-ray source from Ametek, equipped with a tungsten anode (ref. MNX2-911-W), operated at 50 kV and 200 μA, as the excitation source. No X-ray filters were used. The emitted light was collected using a UV optical fiber coupled to a Shamrock SR-500i-D2 imaging spectrograph (Andor). A 149 lines/mm grating, blazed at 300 nm, was used for spectral dispersion. The system was equipped with a Newton EMCCD detector (Andor).

Persistent luminescence decays were measured using a home-built setup inside a Siemens D5000 X-ray diffractometer (Cu anode, unfiltered, operated at 40 kV, 40 mA), yielding an estimated air kerma rate of 15 Gy min^{-1} at the position of the sample. Approximately 5 mg of powder was deposited and compacted in the central round-shaped part (5 mm in diameter and 2 mm in depth) of an aluminum sample holder. An optical fiber was placed 4 cm above the powder and used for the acquisition of RL spectra and persistent luminescence intensity.[41] The spectra were collected using an AvaSpec-HERO, 195–980 nm fiber-coupled spectrometer from Avantes.

Thermally stimulated luminescence (TSL) measurements were conducted in the same custom-built setup as for persistent luminescence measurements. The powders were incorporated into a PDMS layer and mounted in a Linkam FTIRSP600 heating and cooling stage equipped with a Kapton window at the top side and a quartz window at the bottom side. The samples were irradiated for 5 minutes at 83 K prior to TSL recording. Heating was carried out at a rate of 30 K min^{-1}.

3. Results and discussion

a. YPO_4:Ce compounds

A YPO_4:Ce sample was synthesized *via* the MW-assisted hydrothermal method described in the experimental section, with a nominal Ce content of 0.5% relative to the total RE cation content (RE = Y + Ce). The nominal concentrations of precursors introduced in the MW reactor are reported in Table S1. The as-prepared (AP) sample was designated as MW-AP. Half of the sample was subsequently annealed at 1100 °C and is referred to as MW-1 (Table 1). ICP-OES analysis of MW-1 revealed an actual cerium concentration of 0.24% (± 0.04), substantially lower than the nominal value. This discrepancy suggests incomplete incorporation of cerium into the YPO_4 host lattice, likely due to the significant mismatch between the ionic radii of Ce^{3+} (1.143 Å in eightfold coordination) and Y^{3+} (1.019 Å). The unincorporated Ce was likely removed during the washing steps. For comparison, a YPO_4:Ce bulk powder was synthesized *via* a solid-state reaction, also described in the experimental section, with a nominal Ce content of 0.3%. This sample, labelled SSR-1 in

Table 1, exhibited a measured Ce content of 0.35% (± 0.04) by ICP-OES analysis.

The XRD patterns of the three cerium mono-doped samples—MW-AP, MW-1, and SSR-1—are shown in Fig. 1(a). All three exhibit the characteristic diffraction peaks of xenotime, the tetragonal crystal phase of anhydrous YPO_4 (zircon-type structure) with space group $I4_1/amd$ (ICDD PDF n° 84-0335).[42] Recent studies on hydrothermal and solvothermal synthesis have demonstrated that key structural properties, including the degree of crystallinity (amorphous *vs.* crystalline),[28] the nature of the crystal phase (tetragonal YPO_4, monoclinic $YPO_4{\cdot}2H_2O$, and hexagonal $YPO_4{\cdot}0.8H_2O$),[22,28] as well as the morphology and density of the nanoparticles,[29] can be effectively tuned by varying specific synthesis parameters. These parameters include pH, temperature, reaction time, solvent type, and the presence or absence of additives. Specifically, low pH conditions promote the crystallization of the anhydrous tetragonal phase at relatively low temperatures—for example, 130 °C for Tb-doped YPO_4 under hydrothermal conditions[28]—whereas higher pH values tend to favour the formation of the hydrated hexagonal phase.[22] In this work, we optimized our synthesis parameters to 120 °C, 30 minutes, and pH = 0.9. As confirmed by XRD, these conditions successfully yielded the tetragonal anhydrous YPO_4 phase. Although no secondary phases were detected in the diffractogram of the as-prepared sample (MW-AP), annealing led to the appearance of minor impurity peaks at $2\theta = 21.8°$ and $24.4°$ in MW-1. These peaks are attributed to yttrium polyphosphate, $Y(PO_3)_3$ (ICDD PDF n° 36-0255), a crystalline phase characterized by a lower Y/P ratio than that of YPO_4 (Y/P = 1), which tends to be formed in sol–gel synthesis methods as well.[43] This observation might suggest that a portion of the yttrium, which is nominally introduced into the reaction medium, is lost during the final washing steps of the powder. As shown in the zoomed-in view of Fig. 1b, the diffraction peaks of the hydrothermal samples are noticeably broader than those of the solid-state sample. Using the Scherrer formula, we estimated a crystallite size of approximately 29 nm (±2 nm) for MW-AP. Annealing (MW-1) increased the crystallite size slightly to 35 nm (±3 nm), indicating that the crystalline domains grew only marginally during the annealing process of the sample prepared through hydrothermal synthesis. Interestingly, the solid-state sample exhibited a relatively small crystallite size of 59 nm (±3 nm), which is attributed to the particularly poor sinterability previously reported for YPO_4.[44]

Fig. 2 presents the FT-IR spectra of the three cerium mono-doped compounds. In all samples, two sharp bands at 519 cm^{-1} and 638 cm^{-1} are attributed to the antisymmetric bending vibrations of the O–P–O group, while the band near 980 cm^{-1} corresponds to the antisymmetric stretching vibration of the $PO_4{}^{3-}$ group.[27,28] In MW-AP, the band at 1640 cm^{-1} and the broad absorption between 2500 and 3600 cm^{-1} are associated with the bending and stretching vibrations of O–H groups, respectively.[29] These features indicate the presence of surface hydroxyl groups in the as-prepared sample, which are effectively suppressed by the annealing process, as evidenced in the MW-1 spectrum.[45]

Fig. 3 shows SEM (a, c and e) and TEM (b, d and f) images of MW-AP (a and b), MW-1 (c and d), and SSR-1 (e and f). The particle sizes of MW-AP and MW-1 were determined from TEM image analysis of a total of 277 and 291 particles, respectively. The size distributions were plotted as histograms using a bin width of 5 nm and subsequently fitted with the standard log-normal function typically used for particle growth analysis. These histograms, along with the fitted functions and corresponding fitting parameters, are presented in Fig. 3(g) and (h), for MW-AP and MW-1 respectively. The deduced median particle sizes are 55.5 nm and 68.5 nm, for MW-AP and MW-1, respectively, with standard deviations of 16.3 nm and 21.4 nm. The as-prepared sample exhibits lenticular and round-shaped YPO_4 nanoparticles with a median particle size of 55.5 nm, consistent with the crystallite size of ∼33 nm estimated from the Scherrer formula. These morphologies align with previous studies reporting particle shapes ranging from cuboids and nanorods to nano-bullets and rice grains, which can be tuned by parameters such as temperature, pH, and holding time during synthesis.[22,30,31] From the SEM images, an average particle size of ∼60 nm was evaluated, which agrees well with the TEM results and the Scherrer crystallite size. Following annealing, the median particle size increases moderately

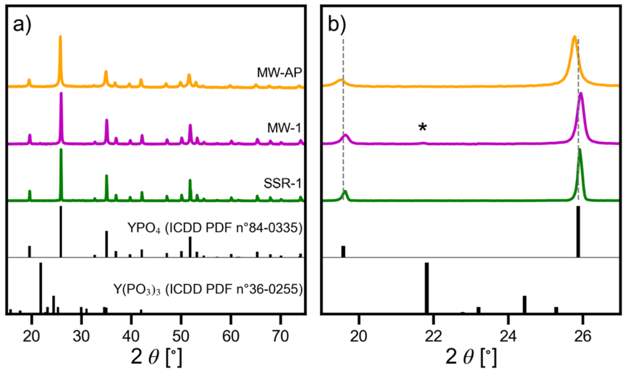

Fig. 1 (a) XRD patterns of cerium-doped yttrium phosphate samples prepared by MW-assisted hydrothermal synthesis and by SSR. (b) Enlarged views.

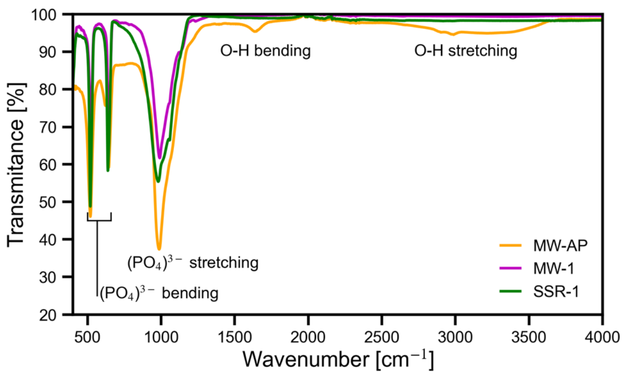

Fig. 2 FTIR spectra of cerium-doped yttrium phosphate samples prepared by MW-assisted hydrothermal synthesis and by SSR.

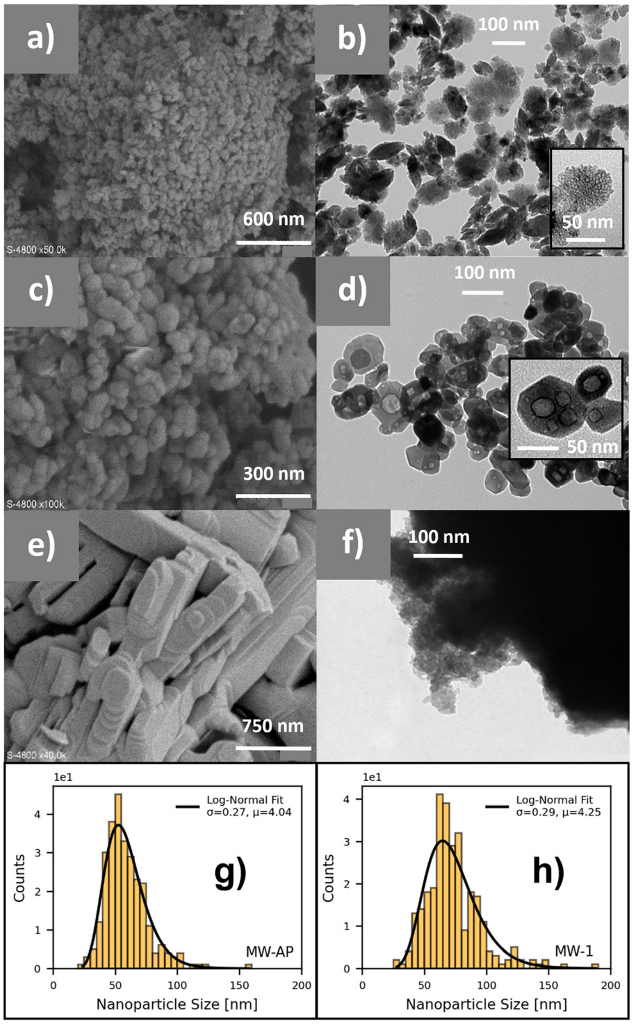

Fig. 3 SEM (a), (c) and (e) and TEM images (b), (d) and (f) of the following cerium-doped yttrium phosphate samples: MW-AP (a) and (b), MW-1 (c) and (d), SSR-1 (e) and (f). Size distribution of MW-AP (g) and MW-1 (h).

(+ 23%) relative to the as-prepared sample from 55.5 nm to 68.5 nm, accompanied by a marked increase in aggregation. The TEM-derived size of 68.5 nm is consistent with SEM observations (∼70 nm). XRD analysis also revealed an increase in crystallite domain size (+21%) from 29 nm to 35 nm.

A magnified view in Fig. 3(b) highlights the mesoporous structure of individual nanoparticles, showing pores approximately 2–5 nm in size. This distinctive feature has been already observed in hydrothermal or solvothermal syntheses of YPO_4.[19,25,30,31,42] Along with annealing, the morphology undergoes a significant transformation: nanoporosity disappears and densification occurs. The particles adopt more well-defined geometrical shapes, often appearing octagonal. TEM images also reveal the presence of internal closed cavities within individual nanoparticles. This unusual feature has previously been reported in tetragonal YVO_4 nanoparticles synthesized hydrothermally.[46] The formation of these cavities may follow a mechanism similar to the coarsening process observed in crystalline nanoporous metals, which involves void bubble formation.[47]

Fig. 3(e) and (f) present SEM and TEM images, respectively, of SSR-1, revealing a microstructure that is markedly different from those of the other two samples. The solid-state reaction product consists of rectangular cuboid particles measuring a few hundred nm in length.[48] TEM analysis (Fig. 3(f)) confirms a fully agglomerated, non-porous structure, composed of 59 nm-large crystallites, according to XRD, and consistent with materials synthesized by solid-state methods.

Physisorption measurements for MW-AP and MW-1 display nitrogen adsorption isotherms, shown in Fig. 4(a), that further confirm the presence of porosity. For MW-AP, a sharp increase in adsorbed N_2 at low relative pressure (P/P_0) indicates the presence of nanopores (diameters < 2 nm)—an effect that is absent in the isotherm of MW-1, suggesting nanopore loss upon annealing. At higher relative pressures ($P/P_0 > 0.8$), both MW-AP and MW-1 exhibit hysteresis loops, which point to a certain degree of mesoporosity that diminishes after annealing. BJH analysis, presented in Fig. 4(b), reveals a shift in pore size distribution, with average pore sizes increasing from ∼15 nm to ∼30 nm post-annealing. This change is attributed to interparticular porosity and is consistent with the particle growth observed with TEM during thermal treatment. These findings are supported by the high specific surface area measured for MW-AP (142 $m^2\ g^{-1}$), which aligns closely with previously reported values (∼145 $m^2\ g^{-1}$) for similar mesoporous lenticular YPO_4 nanoparticles.[32] After annealing, MW-1 shows a reduced specific surface area of 59 $m^2\ g^{-1}$.

The combination of N_2 physisorption data and TEM imaging confirms the presence of both intrinsic nanopores and interparticular mesoporosity in the as-prepared samples. The observed nanoporosity is typically attributed to a crystallization mechanism under hydrothermal/solvothermal conditions, where nucleation begins within nanosticks that aggregate into nanobundles. This process results in nanoporous particles with oblong morphologies such as lenticular, rice grain, or rod-like shapes.[19,32] When combined with sufficient luminescence, such microporosity can be advantageous for biomedical applications—particularly for drug delivery, as has been demonstrated in previous studies.[49,50]

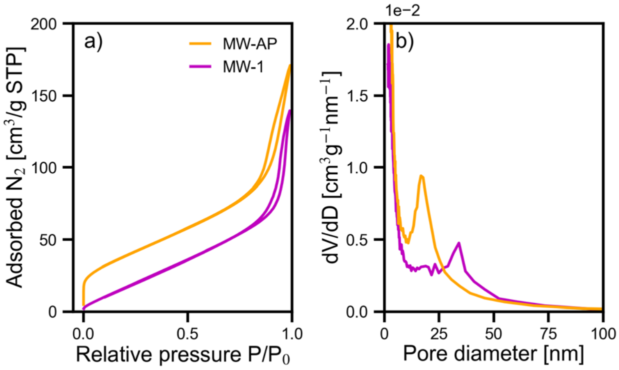

Fig. 4 Nitrogen adsorption–desorption isotherms (a) and pore-size distribution curves (b) of cerium-doped yttrium phosphate samples prepared by MW-assisted hydrothermal synthesis.

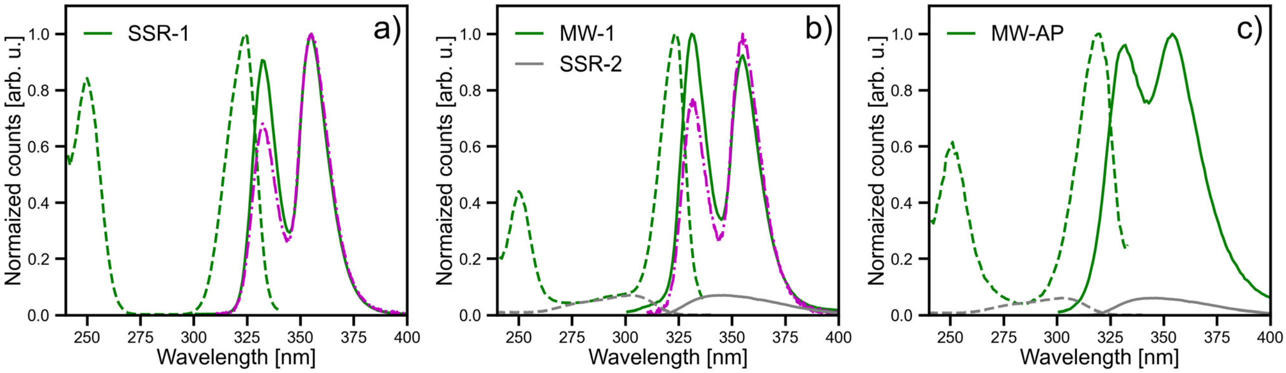

Fig. 5 PL excitation (dashed green) and emission (solid green) spectra, together with RL emission spectra (magenta) of YPO_4:Ce samples prepared by (a) SSR and by MW-assisted hydrothermal synthesis (b) after and (c) before annealing. For comparison, PL excitation and emission spectra of the $Y(PO_3)_3$:Ce sample are shown in grey in panel (b) and (c).

Normalized PL excitation and emission spectra are presented in Fig. 5. The emission spectrum of SSR-1 exhibits the characteristic doublet of Ce^{3+}, corresponding to the transition from the lowest 5d excited state to the spin–orbit split $^2F_{7/2}$ and $^2F_{5/2}$ levels (Fig. 5(a)). These emission bands peak at 331 nm and 355 nm, respectively, reflecting an energy separation of 2040 cm^{-1}, consistent with the expected splitting of the Ce^{3+} 4f ground state. The excitation spectrum reveals two bands centred at 250 nm and 323 nm, attributed to transitions from the 4f states of Ce^{3+} to the two lowest 5d excited states in YPO_4:Ce.[51] The annealed sample prepared *via* hydrothermal synthesis exhibits similar PL emission and excitation features as SSR-1 (Fig. 5(b)). However, a variation in the intensity ratio of the doublet peaks of the PL emission spectrum is observed between SSR-1 and MW-1. This discrepancy is attributed to a slightly higher cerium content in the solid-state compound, as revealed by ICP-OES analysis of the samples (see Table 1). The increased Ce^{3+} concentration enhances self-absorption effects, hence attenuating the intensity of the shorter-wavelength peak (see Fig. S3 for evidence of the self-absorption effect). Additionally, a weak and broad excitation band is observed between 270 nm and 320 nm in MW-1. This feature is assigned to Ce^{3+} ions incorporated within the $Y(PO_3)_3$ impurity phase evidenced by XRD, as shown in Fig. 1. To validate this hypothesis, a $Y(PO_3)_3$:0.5%Ce sample (SSR-2) was synthesized. Its measured PL excitation and emission spectra, shown in grey in Fig. 5(b) and (c), support this assignment (see also Fig. S1). The same weak and broad excitation band between 270 and 320 nm is also observed in Fig. 5(c) for the as-prepared sample. Although no impurity peaks of $Y(PO_3)_3$ are visible in its XRD pattern, we attribute this feature to Ce^{3+} emission from a poorly crystallized $Y(PO_3)_3$ phase, whose diffraction peaks are likely too weak and broadened to be detected. In Fig. 5(c), the as-prepared hydrothermal sample displays similar spectral features to the annealed one, though with broadened bands and a different intensity ratio between the excitation bands at 250 nm and 323 nm. These differences are attributed to a wider distribution of local environments for Ce^{3+} ions. Such a distribution may result from the highly mesoporous nature of the material, which increases the likelihood of Ce^{3+} ions residing near the surface in distorted environments, or alternatively from the reduced crystallinity of the as-prepared sample.[52] For quantitative comparison, the PL emission intensity under 254 nm excitation was integrated over the 300–425 nm range for all three samples. As expected, SSR-1 exhibits the strongest luminescence. MW-1 retains approximately 60% of this intensity, while the as-prepared sample reaches about 30%. The improvement of luminescence yield after annealing the as-synthesized nanoparticles is also observed in other compositions and is often assigned to a decrease in quenching defects.[53] For comparison, YPO_4:Ce nanoparticles reported in the literature and synthesized *via* sol–gel or polyol routes typically showed no observable Ce^{3+} emission unless subjected to thermal treatment at 900 °C.[23,24] This comparison highlights the effectiveness of the hydrothermal synthesis route. Furthermore, the mesoporous architecture of the as-prepared sample might contribute positively by promoting multiple light scattering within the nanocrystals, thereby enhancing the absorption efficiency of the excitation light.[54,55]

Luminescence decay curves under pulsed UV-LED excitation at 325 nm are shown in Fig. 6(a). This excitation wavelength directly promotes Ce^{3+} to its first excited 5d state, without involving energy transfer to or from the host matrix (see energy band diagram in Fig. S2). As a result, the recorded decay profiles reflect the intrinsic luminescence dynamics of Ce^{3+} ions occupying the eight-fold coordinated D2d symmetry sites of Y^{3+}. Both SSR-1 and MW-1 exhibit nearly mono-exponential decay behaviour. However, to enable consistent comparison with other samples—particularly the co-doped ones presented in Section 3b—all decay curves were fitted using a multi-exponential model, with the number of components i left unconstrained. Details of this Laplace fitting procedure are provided in the Supplementary Information. From these fits, effective lifetimes (τ_{eff}) weighed by amplitudes A_i were extracted using the relation:

$$\tau_{\text{eff}} = \frac{\sum_i A_i \cdot \tau_i}{\sum_i A_i}$$

The fitted decay curves and the corresponding τ_{eff} values are shown in Fig. S4. The effective lifetimes obtained for SSR-1 and MW-1 are 17.3 ns and 21.8 ns, respectively. These values are in

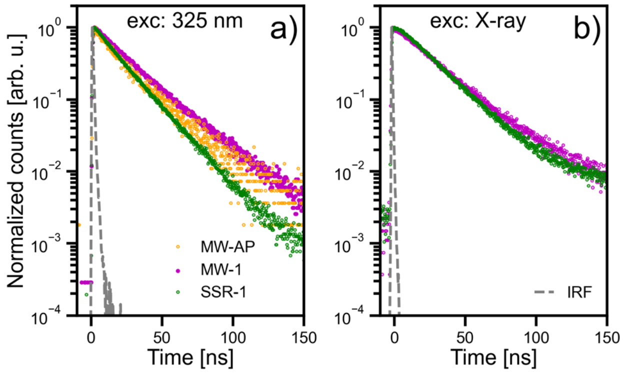

Fig. 6 Luminescence decay curves of cerium-doped yttrium phosphate samples prepared by MW-assisted hydrothermal synthesis and by SSR under (a) pulsed optical excitation at 325 nm and (b) X-ray excitation. The dashed grey line represents the instrument response function (IRF).

good agreement with the previously reported decay time of approximately 25 ns for Ce^{3+} in bulk YPO_4 under UV excitation.10 The observed decrease in τeff from the nanoparticles (MW-1) to the bulk powder (SSR-1), while maintaining an approximately monoexponential decay profile, cannot be explained by known quenching mechanisms. In fact, the trend is opposite to what would typically be expected in the presence of such phenomena. We attribute this behavior of the emitter to variations in the effective refractive index of the surrounding medium. As described by Henderson and Imbusch,[56] the radiative lifetime τ_{rad} is proportional to $f(n)$, a function of the refractive index n, defined as:

$$f(n) = \frac{1}{n}\left(\frac{1}{3}(n^2+2)\right)^{-2}$$

In the case of nanoparticles, it is necessary to consider an effective refractive index that incorporates the influence of the surrounding medium. This concept has been validated in various doped inorganic nanoparticles such as Y_2O_3:Eu[57] and LuAG:Ce.[58] Importantly, it has been demonstrated that the surrounding medium can influence the optical properties up to distances of 100–150 nm from the emitting centre, significantly exceeding the typical size of the nanoparticles themselves.[59] For a composite system comprising two intermixed media, a possible approach is to approximate the effective refractive index n_{eff} by:[57]

$$n_{eff}(x) = x \cdot n_{nano} + (1 - x) \cdot n_{med}$$

where x is the filling factor, representing the volume fraction of the nanoparticle material. Assuming the surrounding medium is air ($n = 1$) and adopting a refractive index of 1.8 for YPO_4,[60] we find that a filling factor of approximately 85% is needed to reproduce the experimentally observed ratio of effective decay times ($\tau_{eff\,MW\text{-}1}/\tau_{eff\,SSR\text{-}1} = 1.26$). In addition to the intrinsic nanoscale effects, this reduced effective refractive index may also reflect the presence of the closed porosity observed by TEM in the nanoparticle samples (Fig. 3(d)).

The as-prepared hydrothermal sample (MW-AP) shows a reduced lifetime of 15.0 ns compared to its annealed counterpart (MW-1). This decrease in lifetime indicates a quenching mechanism that aligns with the observed decrease of the PL light yield in MW-AP relative to MW-1. In addition, the ratio of effective decay times observed between the as-prepared and thermally treated samples suggests that the expected quenching should be approximately 30%. However, under continuous-wave excitation at 254 nm, we observed an intensity ratio of 50%. This discrepancy might indicate that, in addition to quenching, a fraction of cerium ions in the as-prepared sample are inactive and could be Ce^{4+} ions.[61]

Normalized RL spectra under continuous X-ray excitation are presented in Fig. 5(a) and (b) for the SSR-1 and MW-1 samples, respectively, alongside their corresponding PL emission spectra obtained under 254 nm excitation. Although the MW-AP sample exhibited a detectable RL signal, its poor scintillation yield led to a weak signal-to-noise ratio and is therefore not shown here. For the same reason, the X-ray induced decay time has not been measured. For both SSR-1 and MW-1, the RL spectra display the same characteristic 5d–4f transitions observed in the PL spectra. However, self-absorption effects are notably more pronounced under X-ray excitation, owing to the greater penetration depth of X-rays and hence the longer optical pathlength for the generated emission to escape the sample (Fig. S3). As a result, the short-wavelength component of the emission doublet is systematically diminished in intensity.

Integration of the RL signals over the 300–425 nm range reveals a performance disparity between the solid-state and hydrothermal synthesis routes. Specifically, MW-1 achieves only 37% of the RL intensity of SSR-1, while MW-AP yields a mere 0.2%. These findings indicate that unannealed hydrothermal YPO_4:Ce nanoparticles exhibit extremely limited scintillation efficiency and are therefore unsuitable as nanoscintillators in their as-prepared form. Considering that the MW-AP sample exhibits a PL yield approximately half that of the MW-1 sample, the significantly reduced yield under X-ray excitation suggests that the electrons and holes generated through the multiplication processes do not efficiently reach the Ce^{3+} ions. This effect is likely due to strong carrier trapping in the untreated nanoparticles, which presumably contain a high density of defects at the surface.

Luminescence decay times under pulsed X-ray excitation are shown in Fig. 6(b) for SSR-1 and MW-1. Compared to excitation at 325 nm, the decay profiles for both samples exhibit notable differences: a weak rise time flattens the decay curve within the first 10–20 ns, and an additional minor slow decay component appears beyond ∼100 ns. Furthermore, a very flat component is visible beyond 200 ns in the decay curves shown in Fig. S4. This flat component contributes to a slightly elevated baseline preceding $t = 0$, as its timescale exceeds the 250 kHz repetition period of the pulsed X-ray source. Effective lifetimes of 25.1 ns for SSR-1 and 27.3 ns for annealed MW-1 are extracted from the fits (see Fig. S4). They are longer than their UV-excited counterparts, which exhibited lifetimes of 17.3 ns and 21.8 ns, respectively. These extended lifetimes under X-ray excitation are consistent with values reported in the literature, *i.e.* a ∼30 ns scintillation decay time for YPO_4:Ce single crystals under gamma excitation[4] and a ∼33 ns decay time observed in YPO_4:Ce bulk powders under beta excitation.[5] In the scintillation process, X-rays generate free electrons in the conduction band and free holes in the valence band. In an ideal scintillator, these carriers, after thermalization, directly transfer their energy to luminescent centres, resulting in light emission. In our YPO_4:Ce samples, both the observed rise time and the presence of longer decay components suggest the involvement of additional intermediate energy trapping processes.[62,63] Previous studies on YPO_4:Ce have identified such trapping mechanisms evidenced by two TSL peaks: one around 100 K, attributed to hole trapping at certain Ce^{3+} sites and electron trapping at others, and another at 195 K, associated with intrinsic defects in the YPO_4 host lattice.[64,65] These traps hinder the immediate transfer of energy to the emitting Ce^{3+} centres. Thermal detrapping from the 100 K and 195 K traps, *via* either band-assisted mechanisms or thermally activated tunnelling, may contribute to the observed slow decay component. Conversely, the delayed rise time might be explained by athermal or thermally assisted tunnelling from closely spaced defect or dopant pairs.

b. YPO_4:Ce,Ho compounds

Building on predictions from the energy level scheme of lanthanides in YPO_4 (Fig. S2), we previously developed $YPO_4:Pr^{3+},Ho^{3+}$ that exhibited the longest persistent luminescence in the red region among several $YPO_4:Pr^{3+},Ln^{3+}$ compounds (Ln = Nd^{3+}, Dy^{3+}, Ho^{3+}, or Er^{3+}). Given that Ce^{3+}, like Pr^{3+}, has its ground state situated well above the valence band maximum, it is also anticipated to serve as an efficient hole trap and recombination centre under X-ray excitation. Supporting this, Moretti *et al.*[65] reported long-lasting phosphorescence in $YPO_4:Ce^{3+},Nd^{3+}$ single crystals. Their systematic study showed that for a nominal Ce^{3+} concentration of 0.1%, increasing the Nd^{3+} content from 0.01 to 0.1 and subsequently to 0.5 mol% resulted in a proportional enhancement of persistent luminescence intensity. Inspired by these findings and with the aim of optimizing persistent luminescence in Ce-doped YPO_4 nanoparticles, we synthesized a series of Ce,Ho co-doped samples in which the Ho^{3+} concentration exceeded that of Ce^{3+}. Specifically, samples with nominal Ho^{3+} contents of 0.5%, 1%, and 2%, designated as MW-2, MW-3, and MW-4, respectively, were prepared (Table 1). Notably, according to the ICP results, Ho co-doping appears to promote the incorporation of Ce, resulting in a Ce content closer to the nominal value than that observed in the monodoped samples. These co-doped materials displayed similar PL spectral profiles to the mono-doped compounds (Fig. S5). Their relative PL intensities are presented in Fig. 7(a) as a function of their experimental Ho content determined by ICP-OES (Table 1). Increasing the Ho^{3+} concentration from nominal 0 to 2% led to a systematic decrease in both PL and RL yields. It is worth noting that the RL spectra were measured immediately after the X-ray source was turned on, ensuring that no charging effects were involved.

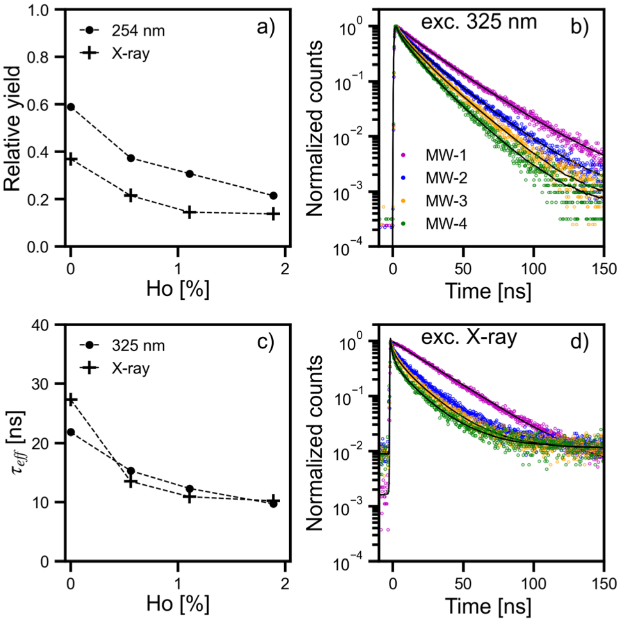

Fig. 7 Relative luminescence yields (a) and effective lifetimes (c) under optical (254 nm for continuous PL and 325 nm for pulsed decay measurements) and luminescence decay curves under pulsed optical (b) and X-ray (d) excitation of YPO_4:0.5 mol% Ce, *x* mol% Ho samples with nominal content *x* = 0 (MW-1), 0.5 (MW-2), 1 (MW-3), and 2 (MW-4). In (a), the value of 1 corresponds to the PL and RL yields of SSR-1 (*x* = 0).

Luminescence decay measurements under 325 nm excitation for the series of co-doped samples are presented in Fig. 7(b). Unlike MW-1, which exhibits an almost mono-exponential decay, the co-doped samples MW-2, MW-3, and MW-4 show increasingly quenched decay profiles as the Ho^{3+} concentration increases. Corresponding fits, obtained using the same methodology applied to the mono-doped compounds, are shown in Fig. S6. The effective lifetimes, plotted in Fig. 7(c), decrease with rising Ho^{3+} content, consistent with the decrease in PL yield. This quenching is likely due to non-radiative energy transfer from excited Ce^{3+} ions to neighbouring Ho^{3+} ions. As reported by others,[66] these Ho^{3+} ions are non-emissive at room temperature in YPO_4. This can be explained by an energy resonance between the emitting levels of Ho^{3+} and the phonon energies of the YPO_4 host matrix.[66] Thus, once excited *via* energy transfer from Ce^{3+}, the Ho^{3+} ions completely transfer their energy to phonons, which dissipate it non-radiatively. As the Ho concentration increases, more Ce^{3+} ions are quenched.

Decay measurements under X-ray excitation for the (Ce,Ho) co-doped samples are presented in Fig. 7(d). Consistent with the observations under 325 nm excitation, these co-doped compounds exhibit increasingly non-exponential decay behaviour and progressively shorter effective lifetimes as the Ho^{3+} concentration increases (Fig. 7(c)). Furthermore, under X-ray excitation, a flat decay component emerges at times longer than 60 ns in the co-doped samples (Fig. S4), leading to a noticeable increase in the background signal before *t* = 0, compared to excitation at 325 nm. Thermal detrapping from the 100 K and 195 K traps, whether through band-assisted mechanisms or thermally activated tunnelling, and from the 325 K trap (electron trapping at Ho^{3+})[64] through thermally assisted tunnelling probably contributes to this flat decay component.

Finally, persistent luminescence measurements were carried out for the four samples with varying Ho^{3+} concentrations. The compounds were subjected to 10 minutes of continuous X-ray irradiation, during which RL spectra were recorded every five seconds. Following the cessation of irradiation, measurements continued at the same interval for an additional 20 minutes. The RL and persistent luminescence signals, integrated over the 300–425 nm range, are plotted as a function of time in Fig. 8. The mono-doped sample MW-1 exhibits almost no detectable persistent luminescence. In contrast, co-doping with 0.5% Ho^{3+} (MW-2) enabled intense persistent luminescence after the irradiation period, confirming predictions regarding the role of Ho^{3+} in shallow electron trapping and delayed recombination in YPO_4:Ce,Ho. This result is in agreement with the expected electron trapping at Ho^{3+} sites in bulk YPO_4:Ce,Ho.[64] This trapping, continuously followed by thermally activated detrapping, also accounts for the progressive increase in RL intensity observed during the charging period in MW-2, the latter being the resultant intensity of RL plus a growing persistent luminescence.[65] Note that the mono-doped sample exhibits a slightly decreasing RL signal, which may indicate a minor degradation process, although this is beyond the scope of the present study.

Increasing the Ho concentration to 1% and 2% had a significant detrimental effect on persistent luminescence. The persistent luminescence not only became less intense, due to quenching effects already observed in PL and RL, but also exhibited a faster persistent luminescence decay, as evidenced in the inset of Fig. 8.

To gain further insight into this behavior, thermally stimulated luminescence (TSL) measurements were performed on the same four samples after X-ray irradiation at 83K (Fig. 9). The cerium mono-doped sample MW-1 exhibits a single dominant peak at 185 K. The co-doped sample with 0.5% Ce and 0.5% Ho (MW-2) shows, in addition to the 185 K peak, also a second peak at 335 K together with a continuously increasing, broad TSL intensity starting at 85 K that returns to zero after the high-temperature peak. The TSL spectra of MW-1 and MW-2 closely resemble those of their bulk counterparts previously reported.[64] These features have been attributed to two distinct electron-trapping mechanisms at different defect sites, while holes are deeply trapped at the luminescence center Ce^{3+} ($Ce^{3+} + h^{+} \rightarrow Ce^{4+}$). The low-temperature peak at 185 K arises from electron trapping at an intrinsic defect of the host-lattice. In contrast, the continuous intensity increase observed over 85–370 K as well as the high-temperature peak at 335 K are both associated with electron trapping at Ho^{3+} ($Ho^{3+} + e^{-} \rightarrow Ho^{2+}$). Their detrapping mechanisms, however, differ: the peak at 335 K is associated with recombination after crossing the energy barrier for detrapping, while the continuous intensity located at lower temperatures is linked to a thermally assisted tunneling process through the barrier. When the Ho content is increased to 1% (MW-3) and 2% (MW-4), the TSL intensity below 300 K increases and shifts to lower temperatures, while the high-temperature peak at 335 K, giving rise to PERL at room temperature, disappears. This indicates that thermally assisted tunneling becomes increasingly dominant, whereas the pathway over the energy barrier is progressively suppressed. In this scenario, Ho^{3+} electron traps are emptied at progressively lower temperatures *via* tunneling, leaving no electrons available for the higher-temperature TSL peak at 335 K. As the Ho content increases, the total TSL intensity increases as well, indicating an increase in the trap concentration up to a concentration of 1% Ho. Finally, at a concentration of 2% Ho, the total TSL Intensity decreases, most likely due to some quenching effect. However, the higher defect concentration reduces the distance between trapping sites, thereby enhancing the probability of tunnelling at the cost of a strongly reduced intensity in the high temperature TSL peak at 335 K which is detrimental for the PERL.[14] We demonstrate that low Ho concentrations are hence better for applications requiring PERL at room temperature.

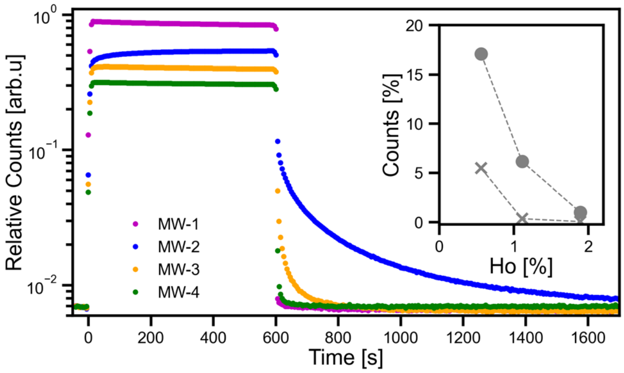

Fig. 8 Time evolution of RL (0–600 seconds) and persistent luminescence (>600 seconds) intensities in YPO_4:0.5 mol% Ce, x mol% Ho samples with nominal Ho content x = 0 (MW-1), 0.5 (MW-2), 1 (MW-3), and 2 (MW-4). Inset: Circles and crosses show persistent luminescence intensity at t = 610 s and t = 700 s, respectively, expressed as a % of the RL intensity at t = 600 s.

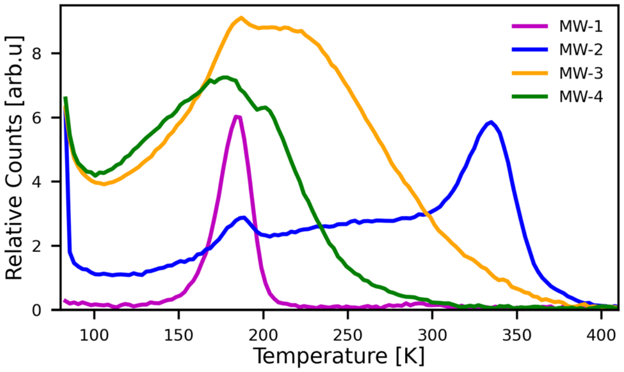

Fig. 9 TSL of YPO_4:0.5 mol% Ce, x mol% Ho samples with nominal Ho content x = 0 (MW-1), 0.5 (MW-2), 1 (MW-3), and 2 (MW-4) recorded at a heating rate of 30 K min^{-1} after irradiation for 5 min at 83 K.

Conclusions

We successfully synthesized nanoporous, photoluminescent Ce-doped YPO_4 nanoparticles, with an initial median diameter of approximately 55 nm, using a hydrothermal method. Subsequent thermal annealing at 1100 °C significantly enhanced their luminescence by densifying the structure—reducing nanoporosity and increasing the particle size slightly to ∼68 nm. After annealing, the nanoparticles demonstrated notable scintillation properties, with a radioluminescence yield reaching 37% of that observed in a bulk reference sample synthesized *via* a solid-state reaction. They also exhibited a fast radioluminescence decay time of 27 ns, along with a slight rise time and a minor slow-decay component. Additionally, co-doping with holmium ions (Ho^{3+}) at a nominal concentration equal to that of cerium (0.5%) imparted persistent luminescence in the UV-A spectral range. Owing to the favourable biocompatibility and aqueous dispersibility of the YPO_4 host matrix, these multifunctional nanoscintillators hold strong potential for biomedical applications. Whether utilized in fast scintillation or persistent luminescence modes, they offer a promising platform for the localized delivery of energetic UV-A emission deep within living tissues, for instance to trigger a photoclick reaction.[67]

Author contributions

PG conducted the majority of the research experiments (syntheses and structural and optical characterization studies). DVdH and PS supervised RL and persistent luminescence measurements and participated in discussion regarding RL and persistent luminescence. CDu carried out luminescence and scintillation decay measurements, performed the fits and participated in discussion regarding PL and RL. MM contributed to the early stages of the project, by performing the initial syntheses and characterization studies. CDo assisted in materials synthesis. JO-D contributed to the discussion on luminescence and applications. PG wrote the first draft of the manuscript. AB supervised the project and wrote the manuscript. All authors contributed to the final preparation of the manuscript.

Conflicts of interest

There are no conflicts to declare.

Data availability

The data that support the findings of this study are available from the corresponding author upon reasonable request.

Supplementary information is available. See DOI: https://doi.org/10.1039/d5cp02667a.

Acknowledgements

This work was supported by the project Emergence@INC from the CNRS and by LabUM Chimie at the University of Montpellier, through funding from the French government managed by the National Research Agency (ANR) under the ''Investissements d'Avenir'' program, reference ANR-16-IDEX-0006. David Van der Heggen acknowledges FWO-Vlaanderen (Fund for Scientific Research-Flanders [1237825N]) for a senior post-doctoral fellowship. The authors acknowledge Pascale Guiffrey (ICGM) for assistance with MW synthesis and Nicolas Brun (ICGM) for physisorption measurements and analysis. They thank the Balard Platform Analysis and Characterization (UAR 2041 PAC Chimie Balard) facilities for technical support. The authors are grateful to Bernard Fraisse for his valuable help with XRD experiments, and Bertrand Rebiere for SEM experiments. The authors thank Sam Koeller and the AETE-ISO platform (OSU-OREME/Université de Montpellier) for ICP measurements.

Notes and references

1 A. Strzelecki, X. Zhao, P. Estevenon, H. Xu, N. Dacheux, R. Ewing and X. Guo, Crystal chemistry and thermodynamic properties of zircon structure-type materials, *Am. Mineral.*, 2024, **109**, 225–242.

2 W. Di, X. Wang, B. Chen, H. Lai and X. Zhao, Preparation, characterization and VUV luminescence property of YPO4: Tb phosphor for a PDP, *Opt. Mater.*, 2005, **27**, 1386–1390.

3 Y. Che, F. Zheng, C. Dou, Y. Yin, Z. Wang, D. Zhong, S. Sun and B. Teng, A promising laser crystal Er^{3+}:YPO_4 with intense multi-wavelength emission characteristics, *J. Alloys Compd.*, 2021, **859**, 157854.

4 I. V. Khodyuk, P. A. Rodnyi and P. Dorenbos, Energy dependence of the relative light output of $YAlO_3$:Ce, Y_2SiO_5:Ce, and YPO_4:Ce scintillators, *Instrum. Exp. Tech.*, 2012, **55**, 187–197.

5 G. N. Dudkin, S. I. Kuznetsov, V. N. Padalko and M. S. Syrtanov, The study of inorganic scintillating materials, *J. Phys.: Conf. Ser.*, 2017, **830**, 012129.

6 K. Kamada, T. Endo, K. Tsutumi, T. Yanagida, Y. Fujimoto, A. Fukabori, A. Yoshikawa, J. Pejchal and M. Nikl, Composition Engineering in Cerium-Doped $(Lu,Gd)_3(Ga,Al)_5O_{12}$ Single-Crystal Scintillators, *Cryst. Growth Des.*, 2011, **11**, 4484–4490.

7 W. Drozdowski, A. J. Wojtowicz, S. M. Kaczmarek and M. Berkowski, Scintillation yield of $Bi_4Ge_3O_{12}$ (BGO) pixel crystals, *Phys. B*, 2010, **405**, 1647–1651.

8 C. M. Pepin, P. Berard, A.-L. Perrot, C. Pepin, D. Houde, R. Lecomte, C. L. Melcher and H. Dautet, Properties of LYSO and recent LSO scintillators for phoswich PET detectors, *IEEE Trans. Nucl. Sci.*, 2004, **51**, 789–795.

9 W. Gyo Lee, D. Hoon Lee, Y. Kyun Kim, J. Kyung Kim and J. Woo Park, Growth and Characteristics of Gd_2SiO_5 Crystal Doped Ce^{3+}, *J. Nucl. Sci. Technol.*, 2008, **45**, 572–574.

10 A. Bril, G. Blasse and J. A. De Poorter, Fast-Decay Phosphors, *J. Electrochem. Soc.*, 1970, **117**, 346.

11 A. J. J. Bos, P. Dorenbos, A. Bessière and B. Viana, Lanthanide energy levels in YPO4, *Radiat. Meas.*, 2008, **43**, 222–226.

12 A. Mandowski and A. J. J. Bos, Explanation of anomalous heating rate dependence of thermoluminescence in

YPO_4:Ce^{3+},Sm^{3+} based on the semi-localized transition (SLT) model, *Radiat. Meas.*, 2011, **46**, 1376–1379.

13 N. R. J. Poolton, R. H. Kars, J. Wallinga and A. J. J. Bos, Direct evidence for the participation of band-tails and excited-state tunnelling in the luminescence of irradiated feldspars, *J. Phys.: Condens. Matter*, 2009, **21**, 485505.

14 A. Dobrowolska, A. J. J. Bos and P. Dorenbos, Electron tunnelling phenomena in YPO_4: Ce,Ln (Ln = Er, Ho, Nd, Dy), *J. Phys. D: Appl. Phys.*, 2014, **47**, 335301.

15 A. Lecointre, A. Bessière, A. J. J. Bos, P. Dorenbos, B. Viana and S. Jacquart, Designing a Red Persistent Luminescence Phosphor: The Example of YPO_4:Pr^{3+},Ln^{3+} (Ln = Nd, Er, Ho, Dy), *J. Phys. Chem. C*, 2011, **115**, 4217–4227.

16 F. Moretti, G. Patton, A. Belsky, M. Fasoli, A. Vedda, M. Trevisani, M. Bettinelli and C. Dujardin, Radioluminescence Sensitization in Scintillators and Phosphors: Trap Engineering and Modeling, *J. Phys. Chem. C*, 2014, **118**, 9670–9676.

17 A. H. Krumpel, A. J. J. Bos, A. Bessière, E. Van Der Kolk and P. Dorenbos, Controlled electron and hole trapping in YPO_4:Ce^{3+},Ln^{3+} and $LuPO_4$: Ce^{3+},Ln^{3+} (Ln = Sm, Dy, Ho, Er, Tm), *Phys. Rev. B:Condens. Matter Mater. Phys.*, 2009, **80**, 085103.

18 A. J. J. Bos, P. Dorenbos, A. Bessière, A. Lecointre, M. Bedu, M. Bettinelli and F. Piccinelli, Study of TL glow curves of YPO_4 double doped with lanthanide ions, *Radiat. Meas.*, 2011, **46**, 1410–1416.

19 S. Majeed, M. Bashir and S. A. Shivashankar, Dispersible crystalline nanobundles of YPO_4 and Ln (Eu, Tb)-doped YPO_4: rapid synthesis, optical properties and bio-probe applications, *J. Nanopart. Res.*, 2015, **17**, 309.

20 Y. Wu, Z. Zhang, H. Suo, X. Zhao and C. Guo, 808 nm light triggered up-conversion optical nano-thermometer YPO_4:Nd^{3+}/Yb^{3+}/Er^{3+} based on FIR technology, *J. Lumin.*, 2019, **214**, 116578.

21 Y. Hu, X. Li, X. Wang, Y. Li, T. Li, H. Kang, H. Zhang and Y. Yang, Greatly enhanced persistent luminescence of YPO_4:Sm^{3+} phosphors via Tb^{3+} incorporation for in vivo imaging, *Opt. Express*, 2020, **28**, 2649.

22 J. Wu, H. Jia, M. Li, H. Jia and Z. Liu, Influence of pH on nano-phosphor YPO_4:2%Sm^{3+} and luminescent properties, *Appl. Phys. A: Mater. Sci. Process.*, 2020, **126**, 87.

23 B. Kahouadji, L. Guerbous, D. J. Jovanović, M. D. Dramićanin, M. Samah, L. Lamiri, L. Benchallal and M. M. Cincović, Annealing effect on the photoluminescence properties of Ce^{3+} doped YPO_4 nanophosphors, *Opt. Mater.*, 2019, **91**, 35–41.

24 H. J. Devi, R. S. Loitongbam and W. R. Singh, Luminescence switching in Ce 3+ ion sensitized YPO_4:Tb^{3+} through Redox reaction, *Mater. Res. Bull.*, 2017, **92**, 74–84.

25 X. Yang, X. Dong, J. Wang and G. Liu, Glycine-assisted hydrothermal synthesis of YPO_4:Eu^{3+} nanobundles, *Mater. Lett.*, 2009, **63**, 629–631.

26 H. Lai, Y. Du, M. Zhao, K. Sun and L. Yang, CTAB assisted hydrothermal preparation of YPO4:Tb^{3+} with controlled morphology, structure and enhanced photoluminescence, *Mater. Sci. Eng., B*, 2014, **179**, 66–70.

27 A. S. Vanetsev, E. V. Samsonova, O. M. Gaitko, K. Keevend, A. V. Popov, U. Mäeorg, H. Mändar, I. Sildos and Yu. V. Orlovskii, Phase composition and morphology of nanoparticles of yttrium orthophosphates synthesized by microwave-hydrothermal treatment: The influence of synthetic conditions, *J. Alloys Compd.*, 2015, **639**, 415–421.

28 A. Garrido Hernández, A. García Murillo, F. D. J. Carrillo Romo, D. Boyer, A. Potdevin, G. Chadeyron and J. R. Miranda, Photoluminescence behavior of YPO_4:Tb^{3+} crystallized in monoclinic, hexagonal or tetragonal phase obtained by hydrothermal process, *Mater. Res. Bull.*, 2016, **84**, 225–231.

29 F. Armetta, V. Boiko, D. Hreniak, C. Mortalò, C. Leonelli, L. Barbata and M. L. Saladino, Effect of hydrothermal time on the forming specific morphology of YPO_4:Eu^{3+} nanoparticles for dedicated luminescent applications as optical markers, *Ceram. Int.*, 2023, **49**, 23287–23294.

30 E. Paradisi, C. Mortalò, V. Zin, F. Armetta, V. Boiko, D. Hreniak, M. Zapparoli, S. M. Deambrosis, E. Miorin, C. Leonelli and M. L. Saladino, Eu-Doped YPO_4 Luminescent Nanopowders for Anticounterfeiting Applications: Tuning Morphology and Optical Properties by a Rapid Microwave-Assisted Hydrothermal Method, *ACS Appl. Nano Mater.*, 2024, **7**, 6893–6905.

31 E. Paradisi, C. Mortalò, V. Zin, S. M. Deambrosis, M. Zapparoli, E. Miorin and C. Leonelli, Understanding the effect of temperature on the crystallization of Eu^{3+}:YPO_4 nanophosphors prepared by MW-assisted method, *Ceram. Int.*, 2025, **51**, 7075–7086.

32 S. Rodriguez-Liviano, F. J. Aparicio, T. C. Rojas and A. B. Hungría, L. E. Chinchilla and M. Ocaña, Microwave-Assisted Synthesis and Luminescence of Mesoporous RE-Doped YPO_4 (RE = Eu, Ce, Tb, and Ce + Tb) Nanophosphors with Lenticular Shape, *Cryst. Growth Des.*, 2012, **12**, 635–645.

33 B. Shao, Y. Feng, S. Zhao, S. Yuan, J. Huo, W. Lü and H. You, Phase-Tunable Synthesis of Monodisperse YPO_4:Ln^{3+} (Ln = Ce, Eu, Tb) Micro/Nanocrystals via Topotactic Transformation Route with Multicolor Luminescence Properties, *Inorg. Chem.*, 2017, **56**, 6114–6121.

34 C. D. McMillen and J. W. Kolis, Hydrothermal synthesis as a route to mineralogically-inspired structures, *Dalton Trans.*, 2016, **45**, 2772–2784.

35 I. Bilecka and M. Niederberger, Microwave chemistry for inorganic nanomaterials synthesis, *Nanoscale*, 2010, **2**, 1358.

36 H. Xiong, J. Dong, J. Yang, Y. Liu, H. Song and S. Gan, Facile hydrothermal synthesis and multicolor-tunable luminescence of YPO_4:Ln^{3+} (Ln = Eu, Tb), *RSC Adv.*, 2016, **6**, 98208–98215.

37 J. Wu, C. Liu, H. Jia, Y. Qi, Z. Liu, Y. Hu and F. Feng, Optical properties, energy transfer and thermal stability of spherical nano-phosphor YPO_4:Eu^{3+}:Sm^{3+}, *J. Lumin.*, 2022, **245**, 118791.

38 Y. Yu, L. Yu, K. Peng, D. Sun, X. Zeng, Y. Deng, Y. Zhao and Y. Xu, Hydrothermal synthesis and tunable luminescence of YPO_4:Eu^{2+}/Eu^{3+},Tb^{3+} nanocrystals, *Ceram. Int.*, 2023, **49**, 29317–29326.

39 B. Wu, J. Wu, S. Wang, Y. Zhang, Q. Lu, Z. Liu, Y. Hu, X. Zhang, J. Li and F. Guo, Synthesis of YPO_4:Tb^{3+} core-shell nanophosphors and their application in fingerprint detection, *Colloids Surf., A*, 2024, **703**, 135373.

40 J. Li, H. Kong, L. Huang, B. Cheng, K. Qin, M. Zheng, Z. Yan and Y. Zhang, Visible Light-Initiated Bioorthogonal Photoclick Cycloaddition, *J. Am. Chem. Soc.*, 2018, **140**, 14542–14546.

41 D. Van der Heggen, D. R. Cooper, M. Tesson, J. J. Joos, J. Seuntjens, J. A. Capobianco and P. F. Smet, Optically Stimulated Nanodosimeters with High Storage Capacity, *Nanomaterials*, 2019, **9**, 1127.

42 Q. Liu, Y. Su, H. Yu and W. Han, YPO_4 nanocrystals: preparation and size-induced lattice symmetry enhancement, *J. Rare Earths*, 2008, **26**, 495–500.

43 S. Lucas, E. Champion, D. Bernache-Assollant and G. Leroy, Rare earth phosphate powders $RePO_4 \cdot nH_2O$ (Re = La, Ce or Y) II. Thermal behavior, *J. Solid State Chem.*, 2004, **177**, 1312–1320.

44 D. Bregiroux, S. Lucas, E. Champion, F. Audubert and D. Bernache-Assollant, Sintering and microstructure of rare earth phosphate ceramics $REPO_4$ with RE = La, Ce or Y, *J. Eur. Ceram. Soc.*, 2006, **26**, 279–287.

45 H. J. Devi, R. S. Loitongbam and W. R. Singh, Luminescence switching in Ce^{3+} ion sensitized YPO_4:Tb^{3+} through Redox reaction, *Mater. Res. Bull.*, 2017, **92**, 74–84.

46 L. Yang, S. Peng, M. Zhao and L. Yu, New synthetic strategies for luminescent YVO_4:Ln^{3+} (Ln = Pr, Sm, Eu, Tb, Dy, Ho, Er) with mesoporous cell-like nanostructure, *Opt. Mater. Express*, 2018, **8**, 3805.

47 J. Erlebacher, Mechanism of Coarsening and Bubble Formation in High-Genus Nanoporous Metals, *Phys. Rev. Lett.*, 2011, **106**, 225504.

48 X. Sun, X. Sun, J. He, X. Li and J. Lv, Synthesis and luminescence of $BiPO_4$:xEu^{3+} powders by solid state reaction method, *Ceram. Int.*, 2014, **40**, 7647–7650.

49 H. Liu and J. Liu, Hollow mesoporous Gd_2O_3:Eu^{3+} spheres with enhanced luminescence and their drug releasing behavior, *RSC Adv.*, 2016, **6**, 99158–99164.

50 X. Liang, J. Fan, Y. Wang, Y. Zhao, R. Jin, T. Sun, M. Cheng and X. Wang, Synthesis of hollow and mesoporous structured $NaYF_4$:Yb,Er upconversion luminescent nanoparticles for targeted drug delivery, *J. Rare Earths*, 2017, **35**, 419–429.

51 L. Van Pieterson, M. F. Reid, R. T. Wegh, S. Soverna and A. Meijerink, $4f^n \rightarrow 4f^{n-1}5d$ transitions of the light lanthanides: Experiment and theory, *Phys. Rev. B:Condens. Matter Mater. Phys.*, 2002, **65**, 045113.

52 T. Yasunaga, M. Kobayashi, K. Oqmhula, H. Qi, T. Ichibha, K. Hongo, S. Yamamoto, R. Maezono, M. Mitsuishi, M. Osada, H. Kato and M. Kakihana, Multiemission of Ce^{3+} from a Single Crystallographic Site Induced by Disordering of Ions, *Inorg. Chem.*, 2024, **63**, 1288–1295.

53 M. N. Da Silva, J. M. De Carvalho, M. C. De Abreu Fantini, L. A. Chiavacci and C. Bourgaux, Nanosized $ZnGa_2O_4$:Cr^{3+} Spinels as Highly Luminescent Materials for Bioimaging, *ACS Appl. Nano Mater.*, 2019, **2**, 6918–6927.

54 Z. Dong, H. Ren, C. M. Hessel, J. Wang, R. Yu, Q. Jin, M. Yang, Z. Hu, Y. Chen, Z. Tang, H. Zhao and D. Wang, Quintuple-Shelled SnO_2 Hollow Microspheres with Superior Light Scattering for High-Performance Dye-Sensitized Solar Cells, *Adv. Mater.*, 2014, **26**, 905–909.

55 B. Zhao, W. Zhao, G. Shao, B. Fan and R. Zhang, Corrosive synthesis and enhanced electromagnetic absorption properties of hollow porous Ni/SnO_2 hybrids, *Dalton Trans.*, 2015, **44**, 15984–15993.

56 B. Henderson and G. F. Imbusch, *Optical spectroscopy of inorganic solids*, Clarendon Press, Oxford University Press, Oxford, New York, 1989.

57 R. S. Meltzer, S. P. Feofilov, B. Tissue and H. B. Yuan, Dependence of fluorescence lifetimes of Y_2O_3:Eu^{3+} nanoparticles on the surrounding medium, *Phys. Rev. B:Condens. Matter Mater. Phys.*, 1999, **60**, R14012–R14015.

58 J. Bárta, V. Čuba, M. Pospíšil, V. Jarý and M. Nikl, Radiation-induced preparation of pure and Ce-doped lutetium aluminium garnet and its luminescent properties, *J. Mater. Chem.*, 2012, **22**, 16590.

59 V. LeBihan, A. Pillonnet, D. Amans, G. Ledoux, O. Marty and C. Dujardin, Critical dimension where the macroscopic definition of refractive index can be applied at a nanometric scale, *Phys. Rev. B:Condens. Matter Mater. Phys.*, 2008, **78**, 113405.

60 G. E. Jellison, L. A. Boatner and C. Chen, Spectroscopic refractive indices of metalorthophosphates with the zircon-type structure, *Opt. Mater.*, 2000, **15**, 103–109.

61 G. Dantelle, D. Testemale, E. Homeyer, A. Cantarano, S. Kodjikian, C. Dujardin, J.-L. Hazemann and A. Ibanez, A new solvothermal method for the synthesis of size-controlled YAG:Ce single-nanocrystals, *RSC Adv.*, 2018, **8**, 26857–26870.

62 F. Moretti, K. Hovhannesyan, M. Derdzyan, G. A. Bizarri, E. D. Bourret, A. G. Petrosyan and C. Dujardin, Consequences of Ca Codoping in $YAlO_3$:Ce Single Crystals, *ChemPhysChem*, 2017, **18**, 493–499.

63 A. J. Wojtowicz, J. Glodo, W. Drozdowski and K. R. Przegietka, Electron traps and scintillation mechanism in YAlO3: Ce and LuAlO3: Ce scintillators, *J. Lumin.*, 1998, **79**, 275–291.

64 A. Lecointre, A. Bessière, A. J. J. Bos, P. Dorenbos, B. Viana and S. Jacquart, Designing a Red Persistent Luminescence Phosphor: The Example of YPO_4:Pr^{3+},Ln^{3+} (Ln = Nd, Er, Ho, Dy), *J. Phys. Chem. C*, 2011, **115**, 4217–4227.

65 F. Moretti, G. Patton, A. Belsky, M. Fasoli, A. Vedda, M. Trevisani, M. Bettinelli and C. Dujardin, Radioluminescence Sensitization in Scintillators and Phosphors: Trap Engineering and Modeling, *J. Phys. Chem. C*, 2014, **118**, 9670–9676.

66 R. Capelletti, A. Baraldi, E. Buffagni, M. Mazzera, N. Magnani, E. M. Rodriguez, J. G. Solé and M. Bettinelli, Optical Spectroscopy of YPO_4 Single Crystals Doped with Ho^{3+}, *Spectrosc. Lett.*, 2010, **43**, 382–388.

67 C. Dujardin, A. Bessière, A. Bulin, F. Chaput and B. Mahler, Inorganic Nanoscintillators: Current Trends and Future Perspectives, *Adv. Opt. Mater.*, 2025, 2402739.